Draft version January 8, 2016
Preprint typeset using LaTeX style emulateapj v. 5/2/11

arXiv:1510.03124v2 [astro-ph.HE] 7 Jan 2016

HYDRODYNAMICAL NUMERICAL SIMULATION OF WIND PRODUCTION FROM BLACK HOLE HOT ACCRETION FLOWS AT VERY LARGE RADII

De-Fu Bu[1], Feng Yuan[1], Zhao-Ming Gan[1], Xiao-Hong Yang[2]

Draft version January 8, 2016

ABSTRACT

Previous works show strong winds exist in hot accretion flows around black holes. Those works focus only on the region close to the black hole thus it is unknown whether or where the wind production stops at large radii. In this paper, we investigate this problem by hydrodynamical simulations. We take into account gravities of both the black hole and the nuclear star clusters. For the latter, we assume that the velocity dispersion of stars is a constant and its gravitational potential $\propto \sigma^2 \ln(r)$, where σ is the velocity dispersion of stars and r is the distance from the center of the galaxy. We focus on the region where the gravitational potential is dominated by the star cluster. We find, same as the accretion flow at small radii, the mass inflow rate decreases inward and the flow is convectively unstable. However, trajectory analysis shows that there is very few wind launched from the flow. Our result, combined with the results of Yuan et al. (2015), indicates that the mass flux of wind launched from hot accretion flow $\dot{M}_{\rm wind} = \dot{M}_{\rm BH}(r/20r_s)$, with $r \lesssim R_A \equiv GM_{\rm BH}/\sigma^2$. Here $\dot{M}_{\rm BH}$ is accretion rate at black hole horizon. R_A is similar to Bondi radius. We argue that the inward decrease of inflow rate is not because of mass loss via wind, but because of convective motion. The disappearance of wind outside of R_A must be because of the change of the gravitational potential, but the exact reason remains to be probed.

Subject headings: accretion, accretion disks − black hole physics − hydrodynamics

1. INTRODUCTION

Hot accretion flow such as advection-dominated accretion flow (ADAFs; Narayan & Yi 1994; 1995; Abramowicz et al. 1995) is an important class of accretion mode because it is now believed to be the standard model of low-luminosity active galactic nuclei, which are the majority of galaxies at least in the nearby universe, and the hard and quiescent states of black hole X-ray binaries (see Yuan & Narayan 2014 for the most updated review of our current theoretical understanding of hot accretion flow and its various astrophysical applications).

One of the most important progresses in this filed in recent years is the finding of the strong wind (real outflow) launched from the accretion flow. The study starts from the pioneer works by Stone et al. (1999, hereafter SPB99) and Igumenshchev & Abramowicz (1999). By performing two-dimensional global hydrodynamical (HD) simulations, they have found that the mass inflow rate (see eq. 11 for definition) decreases with decreasing radius. This study has been extended to simulations with larger radial dynamical range, more spacial dimensions, and inclusion of magnetic field (e.g., Stone & Pringle 2001; Hawley & Balbus 2002; Machida et al. 2001; Pang et al. 2011; Yuan et al. 2012a). In general, it is found that $\dot{M}_{\rm in}(r) \propto r^s$ with $s \sim 0.5-1$ (see a short review in Yuan et al. 2012a). Yuan et al. (2012b, hereafter YBW12) show that the inward decrease of the accretion rate is due to the significant mass loss via wind (see also Narayan et al. 2012; Li et al. 2013; Gu 2015). This conclusion is soon confirmed by the 3 million seconds *Chandra* observation to the accretion flow around the supermassive black hole in the Galactic center, combined with the modeling to the detected iron emission lines (Wang et al. 2013).

By performing the trajectory analysis of virtual test particles in the accretion flow based on the three dimensional general relativistic magneto-hydrodynamic (GRMHD) simulation data of accretion flows, recently Yuan et al. (2015) have analyzed the motion of winds and calculated their various physical properties. The main findings are as follows. Firstly, for a non-rotating black hole, the mass flux of the wind can be described by $\dot{M}_{\rm wind} \approx \dot{M}_{\rm BH}(r/20r_s)$, with $\dot{M}_{\rm BH}$ is the mass accretion rate at the black hole horizon and r_s is the Schwarzschild radius. Secondly, the poloidal speed of wind originating from radius r is $v_p(r) \approx (0.2-0.4)v_K(r)$ where $v_K(r)$ is the Keplerian speed at radius r. The poloidal speed of wind remains roughly unchanged during their outward motion. This is because the centrifugal force and gradient of gas and magnetic pressure can do work to the wind and this work can compensate the gravitational work. Also because of this reason, the initial Bernoulli parameter of wind needs not to be positive. At last, Yuan et al. (2015) find that close to the rotation axis, with $\theta \lesssim 15^\circ$ in the spherical coordinate, the poloidal speed of wind is quasi-relativistic, much higher than that of the other part of wind. This kind of outflow is identified as the "disk-jet" (Yuan & Narayan 2014), which is to discriminate it from the Poynting-flux dominated "Blandford-Znajek" jet. The "disk-jet" or the "BZ-jet", which one corresponds to the observed radio jet remains unclear. All these properties of wind are essential to the study of AGN feedback since wind plays an important role in the feedback process (e.g., Ostriker et al. 2010).

[1] Key Laboratory for Research in Galaxies and Cosmology, Shanghai Astronomical Observatory, Chinese Academy of Sciences, 80 Nandan Road, Shanghai, 200030, China; fyuan@shao.ac.cn
[2] Department of Physics, Chongqing University, Chongqing 400044, China

From the equation $\dot{M}_{\rm wind} = \dot{M}_{\rm BH}(r/20r_s)$, we know that most of the wind comes from the region of large radius. Then a question is how large the value of r can be in the above equation. All numerical simulations of accretion wind so far focus only on the region relatively close to the black hole, so it is difficult for them to answer this question. To answer this question, we have to study the accretion flow far away from the black hole. In this case, the main change is the gravitational potential of the system. In this case, in addition to the potential of the black hole, the gravitational potential of the nuclear star cluster will become important and should be included. We define a radius R_A at which the gravitational force due to the central black hole is equal to that due to the nuclear star cluster. We call R_A to be the boundary of the accretion flow or active galactic nuclei (AGNs). Around R_A, both the depth and slope of the gravitational potential will change compared to the case of a pure black hole potential (see Figure 1). Such a change will potentially change the dynamics of both accretion and wind production. Hereafter, for convenience, we use BHAF to refer the hot accretion flow close to the black hole, and CAAF (circum-AGN accretion flow) to refer the hot accretion flow at large radii, around the boundary of an AGN.

We use numerical simulation to study the wind production in a CAAF. In this paper we do not include magnetic field and focus only on hydrodynamical case. We introduce an anomalous stress to transfer the angular momentum. In reality, it is the magneto-hydrodynamic (MHD) turbulence associated with the magneto-rotational instability (MRI; Balbus & Hawley 1991, 1998) that is responsible for the angular momentum transfer in accretion flows. So MHD simulation is more realistic, which will be our future work. One question of performing HD simulation is then whether the results are realistic. This question has been addressed in YBW12 and Yuan et al. (2015). In YBW12, they have shown that although winds exist in both HD and MHD accretion flows, the mechanisms of wind production are different. In the HD case, the accretion flow is convectively unstable; winds are accelerated by the buoyant force associated with convection, i.e, the gradient of gas pressure. But in the MHD case, the flow is convectively stable; winds are accelerated by the combination of centrifugal force and the gradient of gas and magnetic pressure (Yuan et al. 2015). Even though these differences, the presence of wind seems to be irrelevant to the presence of magnetic field (Begelman 2012). The reason is as follows. In hot accretion flow, radiation can be neglected. Then there are three energy fluxes in the accretion flow. The first flux is the liberation of effective gravitational potential energy. The second is the thermal energy flux transferred by the motion of gas in the accretion flow. The third one is the energy flux transferred by viscosity. If we integrate the energy equation we will have $\dot{M}Be+T\Omega = Q$. In this equation, $\dot{M}$ is the mass accretion rate, Be is the Bernoulli parameter, T is the viscous stress per unit radius, Ω is the angular velocity. $\dot{M}Be$ corresponds to the first and second energy fluxes, $T\Omega$ is the energy flux transferred by viscosity, Q is the net energy flux which is not zero. For a steady state, the net energy flux should be a constant of radius. Therefore, $\dot{M}Be$ and $T\Omega$ should also be constant of radius. Because Be is proportional to $1/r$, $\dot{M}$ is required to be proportional to r. Therefore, basically, it is required that $\dot{M}$ is proportional to r independent of whether the model is hydrodynamic or MHD. Thus, we believe that our result on the wind production based on HD simulation should be same with the MHD case. In addition, academically HD simulation should be useful for us to understand the MHD simulation result.

The structure of the paper is arranged as follows. In §2, we will describe the basic equations and the simulation method. In §3, we will first study the convective stability of CAAFs, then calculate the radial profile of the inflow rate. We will then study whether wind can be produced in CAAFs using the trajectory method. We discuss and summarize our results in §4.

2. METHOD

2.1. *Equations*

In a spherical coordinate (r, θ, ϕ), we solve the following hydrodynamical equations describing accretion:

$$\frac{d\rho}{dt} + \rho\nabla\cdot\mathbf{v} = 0, \tag{1}$$

$$\rho\frac{d\mathbf{v}}{dt} = -\nabla p - \rho\nabla\psi + \nabla\cdot\mathbf{T}, \tag{2}$$

$$\rho\frac{d(e/\rho)}{dt} = -p\nabla\cdot\mathbf{v} + \mathbf{T}^2/\mu. \tag{3}$$

Here, ρ, p, $\mathbf{v}$, ψ, e and $\mathbf{T}$ are density, pressure, velocity, gravitational potential, internal energy and anomalous stress tensor, respectively; $d/dt(\equiv \partial/\partial t + \mathbf{v}\cdot\nabla)$ denotes the Lagrangian time derivative. We adopt an equation of state of ideal gas $p = (\gamma-1)e$, and set $\gamma = 5/3$.

The gravitational potential ψ can be expressed as

$$\psi = \psi_{BH} + \psi_{star}. \tag{4}$$

The black hole potential $\psi_{BH} = -GM_{BH}/(r-r_s)$, where G is the gravitational constant, M_{BH} is the mass of the black hole and r_s is the Schwarzschild radius. We assume that the velocity dispersion of nuclear stars is a constant of radius. This seems to be the case of many AGNs. So the potential of the star cluster is $\psi_{star} = \sigma^2\ln(r) + C$, where σ is the velocity dispersion of stars and C is a constant. So we have

$$R_A = GM_{\rm BH}/\sigma^2. \tag{5}$$

We set $\sigma^2 = 10$ and $G = M_{\rm BH} = 1$ to define our units in the present work. So we have $R_A = 0.1$. Fig. 1 shows the gravitational force distribution.

We use the stress tensor $\mathbf{T}$ to mimic the shear stress. Following SPB99, we assume that the only non-zero components of $\mathbf{T}$ are the azimuthal components,

$$T_{r\phi} = \mu r\frac{\partial}{\partial r}\left(\frac{v_\phi}{r}\right), \tag{6}$$

$$T_{\theta\phi} = \frac{\mu\sin\theta}{r}\frac{\partial}{\partial\theta}\left(\frac{v_\phi}{\sin\theta}\right). \tag{7}$$

This is because the MRI is driven only by the shear associated with orbital dynamics. Other components of the stress are much smaller than the azimuthal components (Stone & Pringle 2001). We adopt the coefficient

of shear viscosity $\mu = \nu\rho$. In models A1, A2, A4 and B, we assume $\nu \propto r^{1/2}$, which is the usual "α" viscosity description (SPB99). In order to study the dependence of results on shear stress, in model A3, we assume $\nu \propto r$. In all models, we set α=0.01 to eliminate the discrepancy due to the magnitude of viscosity coefficient.

2.2. *Initial conditions*

As for the initial density distribution, we assume a rotating equilibrium torus embedded in a non-rotating, low-density medium. We assume that the gas torus has constant specific angular momentum L and assume a polytropic equation of state, $p = A\rho^{\gamma}$, where A is a constant. Using these assumptions, we can integrate the equation of motion into the potential form (Nishikori et al. 2006)

$$\Psi(r,\theta) = \psi + \frac{L^2}{2(r\sin\theta)^2} + \frac{\gamma}{\gamma-1}\frac{p}{\rho} = \Psi(R_0,\pi/2), \quad (8)$$

where R_0 is the radius of density maximum of the torus. Using equation (7), we obtain the density distribution,

$$\rho = \rho_c \left\{ \frac{\max[\Psi(R_0,\pi/2) - \psi(r,\theta) - L^2/(2(r\sin\theta)^2), 0]}{A[\gamma/(\gamma-1)]} \right\}^{1/(\gamma-1)} \quad (9)$$

where ρ_c is the density at the torus center. In this paper, we assume $\rho_c = 1$ and $A = 0.4$.

The ambient medium in which the torus is embedded has density ρ_0 and pressure ρ_0/r. We choose $\rho_0 = 10^{-4}$. The mass and pressure of the ambient medium is negligibly small.

2.3. *Models*

In this paper, we simulate both CAAFs and BHAFs. Models A1-A4 are for CAAFs. In models A1 and A2, we assume viscosity $\nu \propto r^{1/2}$. The only difference between models A1 and A2 is that the resolution of model A2 is two times of that of model A1. In model A3, we set $\nu \propto r$. The purpose to carry out model A3 is to study the dependence of results on viscosity form. To study the boundary effect, we carry out model A4. In model A4, the computational domain is $0.002 < r < 0.4$. In models A1, A2, and A3, the center of the initial torus is located at $r = 1$. In model A4, the center is located at $r = 0.1$ In model B, we simulate a BHAF. Table 1 summarizes all these models.

2.4. *Numerical Method*

We use the ZEUS-2D code (Stone & Norman 1992a,1992b) to solve equations (1)-(3). The polar angle range is $0 \le \theta \le \pi$. We adopt non-uniform grid in the radial direction $(\triangle r)_{i+1}/(\triangle r)_i = 1.037$. The distributions of grids in θ direction in the northern and southern hemispheres are symmetric about the equatorial plane. The resolution at θ in the northern hemisphere is same as that at $\pi - \theta$ in the southern hemisphere.In order to well resolve the accretion disk around the equatorial plane, the resolution is increased from the north and south rotational axis to the equatorial plane with $(\triangle\theta)_{j+1}/(\triangle\theta)_j = 0.9826$ for $0 \le \theta \le \pi/2$ and $(\triangle\theta)_{j+1}/(\triangle\theta)_j = 1.0177$ for $\pi/2 \le \theta \le \pi$. At the poles, we use axisymmetric boundary conditions. At the inner and outer radial boundary, we use outflow boundary conditions.

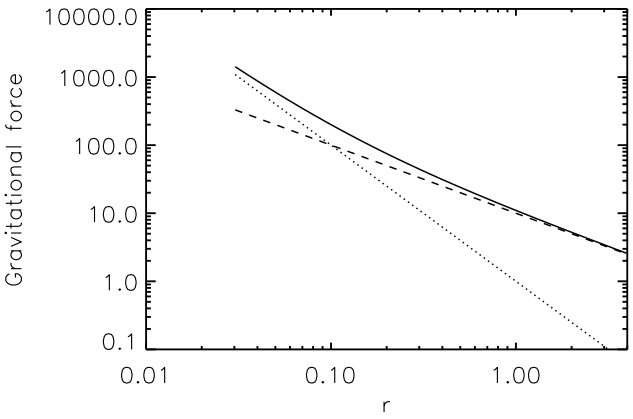

FIG. 1.— The distribution of gravitational force. The dashed and dotted lines correspond to the gravitational force of nuclear star cluster and black hole, respectively. The solid line is their sum.

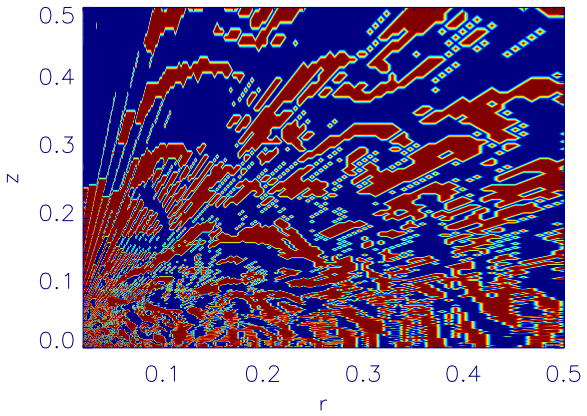

FIG. 2.— Convective stability analysis of Model A1. The result is obtained according to eq. (10) based on the simulation data at t=13.2 orbits at the initial torus center $r = 1$. The red region is unstable.

3. RESULTS

3.1. *Convective stability*

HD simulations of BHAFs (e.g., SPB99; Igumenshchev & Abramowicz 1999, 2000; Yuan & Bu 2010) have found that the flows are convectively unstable, consistent with what has been suggested by the one-dimensional analytical study of BHAFs (Narayan & Yi 1994). The physical reason is that the entropy of the flow increases inward, which is resulted by the viscous heating and negligible radiative loss. As we state in §1, YBW12 shows that strong winds are produced in HD accretion flow around a black hole. The force driving the wind is mainly the buoyant force associated with the convective instability.

To study whether the CAAF is convectively stable or not, we use the Høiland criteria (e.g., Tassoul 1978;

TABLE 1
MODELS IN THIS PAPER

Models	Shear stress	Resolution	Computational domain	Gravitational potential
A1	$\nu \propto r^{1/2}$	334×160	$0.02 \leq r \leq 4$	Star cluster gravity + Black hole gravity
A2	$\nu \propto r^{1/2}$	668×320	$0.02 \leq r \leq 4$	Star cluster gravity + Black hole gravity
A3	$\nu \propto r$	334×160	$0.02 \leq r \leq 4$	Star cluster gravity + Black hole gravity
A4	$\nu \propto r^{1/2}$	334×160	$0.002 \leq r \leq 0.4$	Star cluster gravity + Black hole gravity
B	$\nu \propto r^{1/2}$	334×160	$2r_s \leq r \leq 400r_s$	Black hole gravity

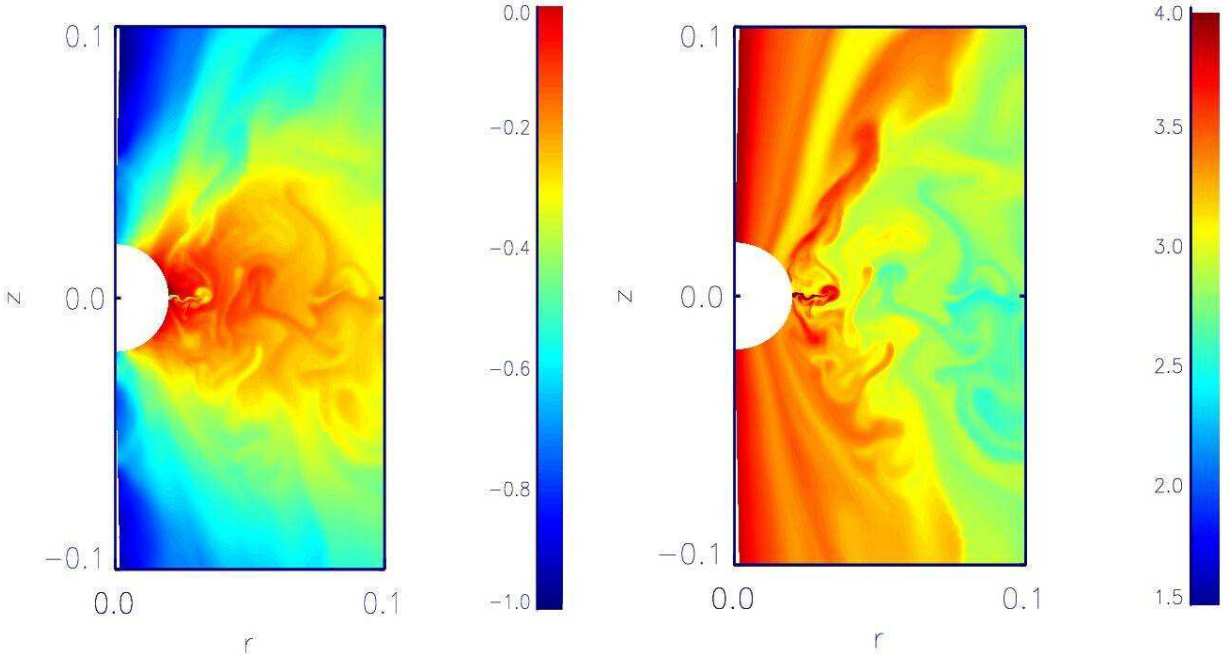

FIG. 3.— Images of the logarithm density (left-panel) and entropy (right-panel) for model A1 at time $t = 12.7$ orbits. Note the correlation between regions of high (low) density and low (high) entropy near the equatorial plane.

Begelman & Meier 1982):

$$(\nabla s \cdot \mathbf{dr})(\mathbf{g} \cdot \mathbf{dr}) - \frac{2\gamma v_\phi}{R^2}[\nabla(v_\phi R) \cdot \mathbf{dr}]dR < 0. \quad (10)$$

In equation (10), $R = r\sin\theta$ is the cylindrical radius, $\mathbf{dr} = dr\hat{r} + rd\theta\hat{\theta}$ is the displacement vector, $s = \ln(p) - \gamma\ln(\rho)$ is $(\gamma - 1)$ times the entropy, $\mathbf{g} = -\nabla\psi + \hat{R}v_\phi^2/R$ is the effective gravity, and v_ϕ is the rotational velocities. For non-rotating flow, this condition is equivalent to an inward increase of entropy, which is the well-known Schwarzschild criteria.

Taking model A1 as an example, Figure 2 shows the result. The result is obtained according to eq. (10) based on the simulation data at t=13.2 orbits at the initial torus center $r = 1$ (here and hereafter, we use the orbital period at the center of initial torus as the time unit). At $t = 13.2$ orbits, the flow has achieved a steady state since the net accretion rate averaged between $t = 12.7$ to 15 orbits is a constant of radius (see figure 4, the dotted line). The red regions are convectively unstable. So we can see that CAAF is mainly convectively unstable. The physical reason for the instability is same as for the BHAF. That is, during the accretion process, viscous heating produces entropy, while the loss of entropy by radiative cooling is neglected. Figure 3 shows the snapshot for logarithm density (left-panel) and entropy $S = \ln(p/\rho^\gamma)$ (right panel) for model A1 at time $t = 12.7$ orbits. From the poles to the equator, the density is strongly stratified. On small scales, large-amplitude fluctuations associated with convection dominate. The entropy plot shows that entropy is maximum along the poles and smallest along the equator. On small scales, bubbles and filaments associated with convection dominate the image. Comparison of the two images demonstrates that regions of high den-

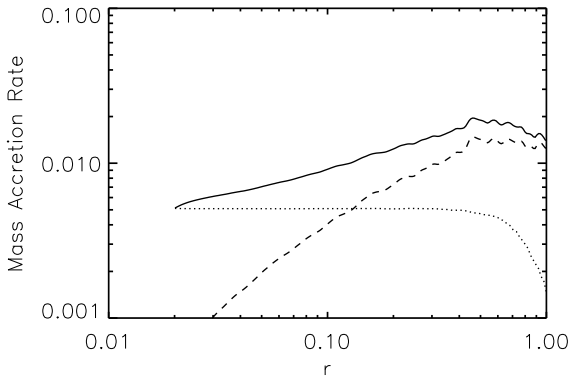

FIG. 4.— The radial profiles of the time-averaged (from $t = 12.7$ to 15 orbits) and angle integrated mass inflow rate $\dot{M}_{\rm in}$ (solid line), outflow rate $\dot{M}_{\rm out}$ (dashed line), and the net rate $\dot{M}_{\rm acc}$ (dotted line) in model A1.

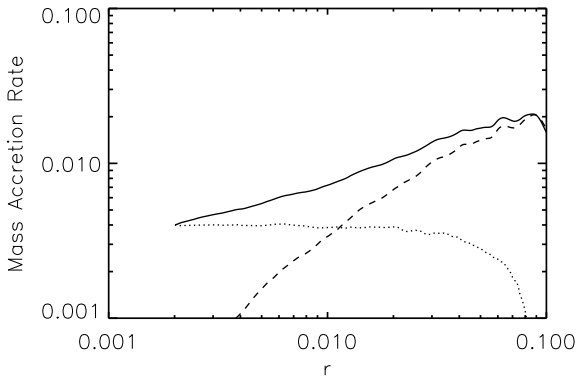

FIG. 5.— The radial profile of the time-averaged (from $t = 4.5$ to 6.8 orbits) and angle integrated mass inflow rate $\dot{M}_{\rm in}$ (solid line), outflow rate $\dot{M}_{\rm out}$ (dashed line), and the net rate $\dot{M}_{\rm acc}$ (dotted line) in model A4.

sity have low entropy, while bubbles of low density have high entropy. This is the typical feature of convection.

3.2. *Mass inflow rate*

Following SPB99, we define the mass inflow and outflow rates, $\dot{M}_{\rm in}$ and $\dot{M}_{\rm out}$, as follows,

$$\dot{M}_{\rm in}(r) = 2\pi r^2 \int_0^\pi \rho \min(v_r, 0) \sin\theta d\theta \qquad (11)$$

$$\dot{M}_{\rm out}(r) = 2\pi r^2 \int_0^\pi \rho \max(v_r, 0) \sin\theta d\theta \qquad (12)$$

The net mass accretion rate is,

$$\dot{M}_{\rm acc}(r) = \dot{M}_{\rm in}(r) + \dot{M}_{\rm out}(r) \qquad (13)$$

Note that the above rates are obtained by time-averaging the integrals rather than integrating the time averages.

Figure 4 shows the time-averaged (from 12.7-15 orbits) and angle-integrated mass accretion rate in model A1. The radial profile of the inflow rate from $r = 0.02$ to 0.4 can be described by

$$\dot{M}_{\rm in} \propto r^{0.42}. \qquad (14)$$

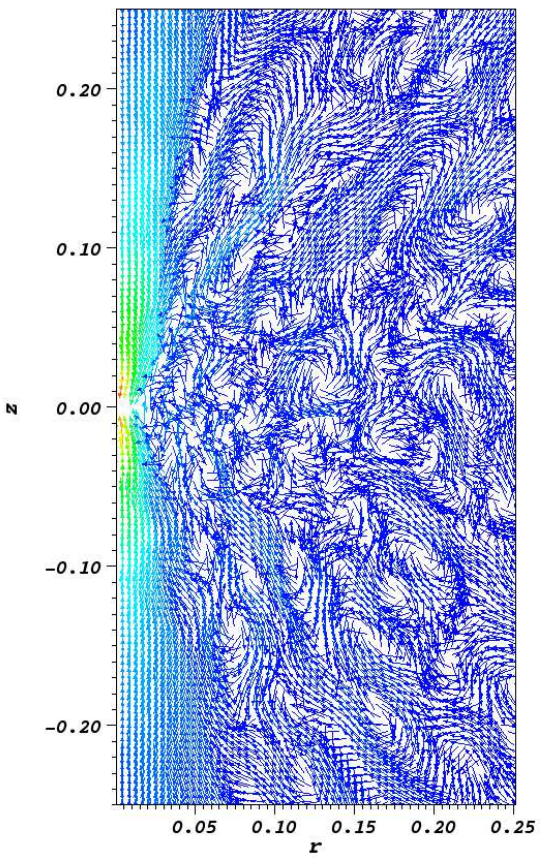

FIG. 6.— Snapshot of velocity vector of model A1 at $t = 12.7$ orbits. Convective eddies occupy the whole domain and it is hard to find winds.

As a comparison, HD simulations of BHAF with a large radial dynamical range by Yuan et al. (2012a) find $\dot{M}_{\rm in} \propto r^{0.54}$ in the model with the same value of α.

In the region $0.02 < r < 0.1$, the outflow rate is much smaller than the mass inflow rate. This region is dominated by the gravity of black hole. Previous works (Yuan et al. 2012b; Yuan et al. 2015) have shown that in this case outflow (wind) should be strong. The apparent discrepancy between this work and our previous works is due to the fact that the region $r < 0.1$ is too close to the inner boundary where a somewhat "unphysical" boundary condition (i.e., outflow condition) is adopted. The result will be reliable if we focus on region far away from the inner boundary. In order to illustrate this point, we have carried out model A4. In this model, our computational domain is $0.002 < r < 0.4$. The result is shown in figure 5. In the region $0.01 < r < 0.1$ which is far away from the inner boundary, the outflow rate obviously becomes very high, which is consistent with our previous works.

3.3. *Does strong wind exist in a CAAF?*

Figure 4 shows that there is a significant mass outflow rate. But this does not mean it is real outflow (wind) because it may be due to the convective turbulent mo-

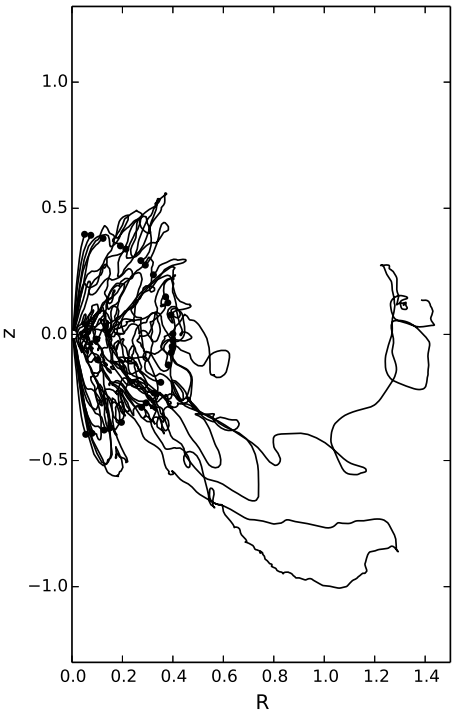

FIG. 7.— Trajectory of gas for model A1. The black dots located at $r = 0.4$ is the starting points of the test particles. Winds are very weak.

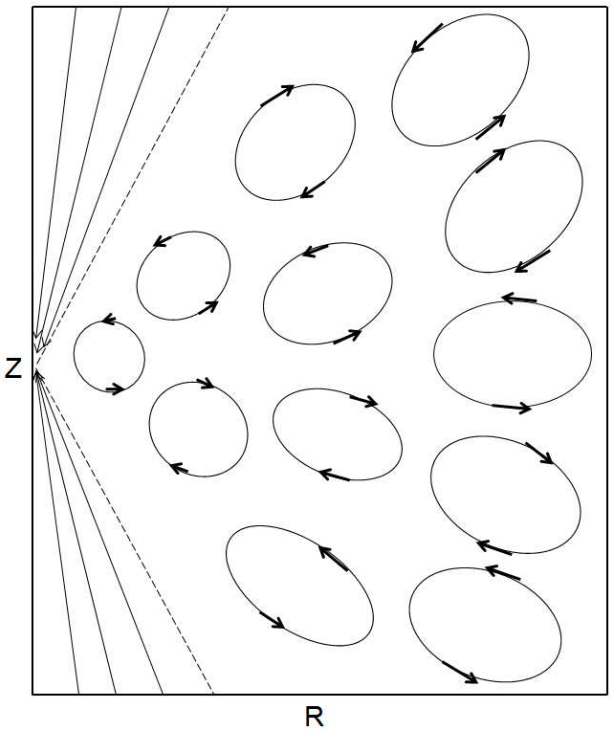

FIG. 8.— Schematic figure of the flow motion in a CAAF. Close to the poles, there is systematic inflow. Away from the poles, the flow is convection dominated. The inward decrease of inflow rate is because the convective mass flux decrease inward.

tion. The turbulence is induced by convective instability so we call the turbulence "convective turbulence". To study whether wind exists, let us first directly look at the velocity field shown in Figure 6. Clearly, convective eddies occupy the whole domain. From equatorial plane to the pole, the scale of convective eddies becomes larger. From large to small radii, the scale of convective eddies becomes smaller. From this figure, it is hard to find winds.

Following Yuan et al. (2015), we now use the much more precise trajectory method to study whether winds exist. The details of this approach can be found in Yuan et al. (2015), here we only briefly introduce it. Trajectory is obtained by connecting the positions of the same "test particle" at different time. This concept is related with the Lagrangian description of fluid. Note that this is different from the streamline which is obtained by connecting the velocity vector of different test particles with infinitely short distance at a given time. This concept is associated with the Euler description of fluid motion. Trajectory is only equivalent to the streamline for strictly steady motion, which is not the case for accretion flow since it is always turbulent. To get the trajectory, we first need to choose some virtual "test particle" in the simulation domain. They are of course not real particles, but some grids representing fluid elements. Their locations and velocity at a certain time t are obtained directly from the simulation data. We can then obtain their location at time $t + \delta t$ from the velocity vector and δt. We do this work using a software called "VISIT".

Using this trajectory approach, we can discriminate easily which particles are real outflows (i.e., winds) and which are doing turbulent motions. We can also calculate the mass fluxes of wind and turbulent outflow by combining with the information of density and velocity of wind. For details, see Yuan et al. (2015). Figure 7 shows the trajectory of 25 "test particles" starting from $r = 0.4$ in model A1. From this figure we can see that the real wind trajectories, i.e., the trajectories which extend from $r = 0.4$ to large radius and never come across $r = 0.4$ twice, are very few. This implies that the mass flux of wind is very small. Our quantitative calculation confirms this result. For example, we find that at $r = 0.4$, the ratio of mass flux of real outflows to the total outflow rate calculated by equation (12) is only 0.3%. This result means that there is almost no wind. As a comparison, in the case of BHAF, Yuan et al. (2015) find that this ratio is $\sim 60\%$.

3.4. *Why the inflow rate decreases inward in a CAAF?*

If the wind is absent, what is the reason for the inward decrease of inflow rate? Guided by our numerical simulation data, we draw a schematic figure of the motion of the flow in Figure 8. We find that systematic real inflow occurs mainly close to the poles. Away from the poles, the flow is full of convective eddies. This reminds us the scenario of convection-dominated accretion flow (CDAF) proposed by Narayan et al. (2000) and Quataert & Gruzinov (2000), although their model was proposed to explain the dynamics of BHAFs rather than CAAFs[3].

[3] YBW12 and Narayan et al. (2012) have shown that the CDAF scenario may be not applicable to BHAFs.

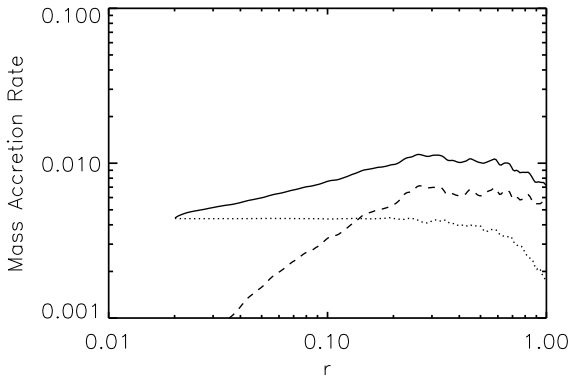

FIG. 9.— The radial profile of the time-averaged (from $t = 21$ to 26 orbits) and angle integrated mass inflow rate $\dot{M}_{\rm in}$ (solid line), outflow rate $\dot{M}_{\rm out}$ (dashed line), and the net rate $\dot{M}_{\rm acc}$ (dotted line) in model A3.

Following Narayan et al. (2000) we now try to understand quantitatively why the inflow rate decreases inward. The mass inflow rate can be estimated by adding up all the inflowing gas elements. This would give $\dot{M}_{\rm in} \sim 4\pi\rho\omega RH/2$, with R being the radius in cylindrical coordinates, H is the half thickness of the flow, ω is the rms velocity of the turbulent eddy. Narayan et al. (2000) shows that $\omega \propto v_k$, where v_k is the Keplerian velocity of the flow. In model A1, we found that $\rho \propto r^{-0.5}$. For the specific gravitational potential we adopt, the Keplerian velocity outside and inside of $r = 0.1$ follows $v_k \propto r^0$ and $v_k \propto r^{-0.5}$, respectively. Therefore, $\dot{M}_{\rm in} \propto \rho r^2 \omega \propto r$ or $r^{\frac{3}{2}}$, i.e., the mass inflow rate increases outward. Of course, such a rough estimation can't explain quantitatively the simulation result of eq. 13.

3.5. *Dependence on model parameters*

3.5.1. *The form of shear stress*

In order to study whether the results depend on the form of shear stress, we have carried out model A3. The only difference between models A1 and A3 is the form of shear stress. In model A3, we assume the shear stress $\nu \propto r$. For model A3, we also find that the flow is convectively unstable. The snapshot of density and entropy of model A3 is very similar to that in model A1. Also, we find that the mass inflow rate is a function of radius. Figure 9 shows the mass accretion rates for model A3. The radial profile of the inflow rate from $r = 0.02$ to 0.4 can be described by

$$\dot{M}_{\rm in} \propto r^{0.4} \tag{15}$$

From Figure 9, we can see a significant mass outflow rate. In order to study whether the outflow rate is dominated by real outflow, we have also plotted the snapshot of velocity vector for model A3. The result is very similar to that of model A1, i.e., full of convective eddies. Trajectory analysis have also been performed to study whether there are strong winds. We find at $r = 0.2, 0.4$, the ratio of mass flux of winds to the total outflow rate calculated by equation (12) is $0.1\%, 0.2\%$, respectively. Again, there is almost no real outflows.

3.5.2. *Resolution*

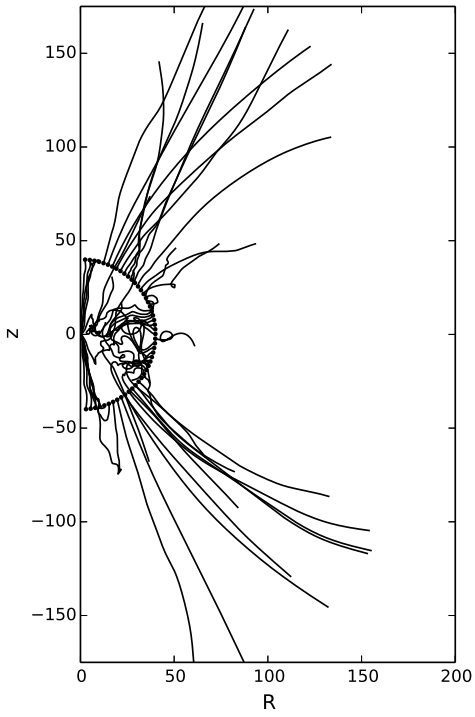

FIG. 10.— Trajectory of gas for model B. The black dots located at $r = 40r_s$ are the starting points of the test particles. Significant winds are clearly present. The horizontal and vertical axis are in unit of r_s.

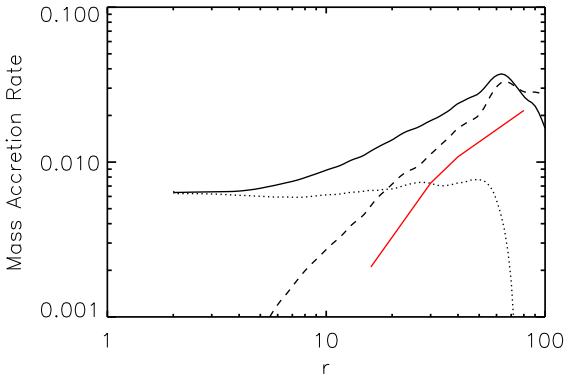

FIG. 11.— The radial profile of the time-averaged (from $t = 1.5$ to 2 orbits) and angle integrated mass inflow rate $\dot{M}_{\rm in}$ (solid line), outflow rate $\dot{M}_{\rm out}$ (dashed line), and the net rate $\dot{M}_{\rm acc}$ (dotted line) in model B. The red line corresponds to the mass flux of wind. The horizontal axis is in unit of r_s.

In order to test whether the results obtained in this paper depend on resolution, we have carried out model A2. In model A2, the number of grids is 668×320, the resolution is two times higher than that of model A1.

In model A2, the flow is still convectively unstable. Again, we find that the mass outflow rate is dominated by convective outflows. Using the trajectory method, we find that the ratio between the real outflows to the total

outflows is $\sim 0.1\%$.

3.5.3. *The gravitational potential*

Previous works have shown that strong winds are present in BHAFs (e.g. YBW12; Li et al. 2013)[4]. In this paper, we have also performed simulations of BHAF. In model B, we simulate the BHAF very close to the black hole, from 2 to $400r_s$. For such a region so close to the black hole, the gravity of the nuclear star cluster can be neglected.

We have performed the trajectory analysis for model B. The results are shown in Figure 10. Clearly, significant winds are present. Figure 11 shows the profile of mass accretion rate. The red line in the figure corresponds to the mass flux of winds. We find that this flux is approximately 70% of the total mass outflow rate calculated from eq. (11). In Yuan et al. (2015), we have studied the MHD BHAFs around a Schwarzschild black hole and found that the ratio between the wind flux to the total outflow rate is $\sim 60\%$. So the results of HD and MHD simulations are similar. From $40-80r_s$, the radial profile of the real outflow rate (wind mass flux) can be described as

$$\dot{M}_{\rm real} \propto r^{0.95} \tag{16}$$

In Yuan et al. (2015), the radial profile of the real outflow mass flux is $\dot{M}_{\rm real} \propto r$. The consistency between the present HD simulation and the MHD simulation of Yuan et al. (2015) supports our HD simulation study of wind as a good approximation of the more realistic MHD study. The underlying physical reason of the consistency between them is discussed in Begelman (2012).

4. CONCLUSION AND DISCUSSION

In previous works, it has been shown that strong winds exist in black hole hot accretion flow (e.g., YBW12). The mass flux of wind follows $\dot{M}_{\rm wind} = \dot{M}_{\rm BH}(r/20r_s)$ (Yuan et al. 2015). In this paper, we have investigated what the value of r can be, i.e., whether or where the wind production will stop., by performing hydrodynamical simulations. The key difference between the present work and the previous ones is that we must include the gravitational potential of the nuclear star cluster in addition to the black hole potential at such large radii. We call the accretion flow in the two regions where the potential is dominated by the nuclear star cluster or by the black hole potential "circum-AGN accretion flow" (CAAF) and "black hole accretion flow" (BHAF), respectively. We find that same as BHAFs, CAAFs are also convectively unstable and the inflow rate is also a power law function of radius. However, different from a BHAF, there is almost no wind in a CAAF. For CAAFs, the inward decrease of inflow rate is not because of strong wind, which is the case of a BHAF, but because the motion is dominated by convection. This scenario is similar to the convection-dominated accretion flow (CDAF) proposed by Narayan et al. (2000) and Quataert & Gruzinov (2000), although the CDAF model is proposed to describe BHAFs rather than CAAFs.

This result indicates that the wind production stops at the radius R_A (refer to eq. 5), where the gravity of the black hole and that of the nuclear star cluster equal to each other. Combining it with the result of Yuan et al. (2015), the mass flux of wind is described by:

$$\dot{M}_{\rm wind} = \dot{M}_{\rm BH}(r/20r_s), \quad r \lesssim R_A. \tag{17}$$

$\dot{M}_{\rm wind} = \dot{M}_{\rm BH}(R_A/20r_s)$ when $r \gtrsim R_A$. It is interesting to compare R_A with the Bondi radius, $R_B(\equiv GM_{\rm BH}/c_s^2)$, which is generally regarded as the outer boundary of the accretion flow. Here c_s is the sound speed of the accreting gas at the Bondi radius. Its typical value is $c_s \equiv \sqrt{\gamma p/\rho} \sim 300(T_{\rm ISM}/10^7K)^{1/2}{\rm km\ s^{-1}}$, with $T_{\rm ISM}$ being the temperature of the interstellar medium around the Bondi radius. This is very close to the typical value of σ, which is $\sim (100-400){\rm km\ s^{-1}}$ (e.g., Kormendy & Ho 2013). So in practice, we can assume that wind stops to be produced outside of the outer boundary of the accretion flow.

The disappearance of winds in CAAFs must be due to the change of the gravitational potential. Specifically, we speculate that it is very likely because of the change of the slope rather than the absolute value of the gravitational potential. In this context we note that the change of differential rotation of the accretion flow, which could be due to the change of the slope of the gravitational potential, causes the change of magnetorotational instability (e.g., Pessah et al. 2008; Penna et al. 2013). But the exact reason still remains to be probed.

ACKNOWLEDGEMENTS

We thank Ramesh Narayan for helpful discussions. This work was supported in part by the National Basic Research Program of China (973 Program, grant 2014CB845800), the Strategic Priority Research Program The Emergence of Cosmological Structures of the Chinese Academy of Sciences (grant XDB09000000), and the Natural Science Foundation of China (grants 11103061, 11133005, 11121062, and 11573051). This work has made use of the High Performance Computing Resource in the Core Facility for Advanced Research Computing at Shanghai Astronomical Observatory.

REFERENCES

Abramowicz M. A., Chen X., Kato S., Lasota J. P., Regev O., 1995, ApJ, 438, L37
Balbus S. A., Hawley J. F., 1991, ApJ, 376, 214
Balbus S. A., Hawley J. F., 1998, Rev. Mod. Phys., 70,1
Begelman, M. C. & Meier, D. L. 1982, ApJ, 253, 873
Begelman M., 2012, MNRAS, 420, 2912
Gu W. M., 2015, ApJ, 799, 71
Hawley J. F., Balbus S. A., 2002, ApJ, 573, 738
Igumenshchev I. V., Abramowicz M. A., 1999, MNRAS, 303, 309
Igumenshchev I. V., Abramowicz M. A., 2000, ApJS, 130, 463
Kormendy J. & Ho L. C. 2013, ARA&A, 51, 511
Li J., Ostriker J., Sunyaev R., 2013, ApJ, 767,105
Machida M., Matsumoto R., Mineshige S., 2001, PASJ, 53, L1
Narayan R., Yi I., 1994, ApJ, 428, L13
Narayan R., Yi I., 1995, ApJ, 452, 710
Narayan R., Igumenshchev I. V., Abramowicz M. A., 2000, ApJ, 539, 798
Narayan R., Sadowski A., Penna R. F., Kulkarni A. K., 2012, MNRAS, 426, 3241
Nishikori H., Machida M., Matsumoto R., 2006, ApJ, 641, 862
Ostriker J. P., Choi E., Ciotti L., Novak G. S., Proga D., 2010, ApJ, 722, 642

[4] Narayan et al. (2012) find much weaker wind. The discrepancy between YBW12 and Narayan et al. (2012) was analyzed in Yuan et al. (2015).

Pang B., Pen U.-L., Matzner C. D., Green S. R., Liebendorfer M., 2011, MNRAS, 415,
Penna, R. F., Sadowski A., Kulkarni A. K., & Narayan R. 2013, MNRAS, 428, 2255
Pessah M. E., Chan C., & Psaltis D. 2008, MNRAS, 383, 683
Quataert E., Gruzinov A., 2000, ApJ, 539, 809
Stone J. M., Norman M. L., 1992a, ApJS, 80, 753
Stone J. M., Norman M. L., 1992b, ApJS, 80, 791
Stone J. M., & Pringle J. E., 2001, MNRAS, 322, 461
Stone J. M., Pringle J. E., & Begelman M. C. 1999, MNRAS, 310, 1002
Tassoul, J.-L. 1978, Theory of Rotating Stars (Princeton: Princeton Univ. Press)
Wang Q. D., Nowak M. A., Markoff S. B., et al. 2013, Sci, 341, 981
Yuan F., Bu D., 2010, MNRAS, 408, 1051
Yuan F., Bu D., Wu M., 2012b, ApJ, 761, 130
Yuan F., Wu M., Bu D., 2012a, ApJ, 761, 129
Yuan F., Gan Z. M., Narayan R., Sadowski A., Bu D. F., Bai X. N., 2015, ApJ, 804, 101
Yuan F., Narayan R., 2014, ARA&A, 52, 529